Materials Science and Engineering B 308 (2024) 117550

Contents lists available at ScienceDirect

Materials Science & Engineering B

journal homepage: www.elsevier.com/locate/mseb

Study of structural, elastic, electronic, optical, magnetic and thermoelectric characteristics of Hexafluoromanganets A_2MnF_6 (A = Cs, Rb, K) cubic double perovskites

K. Bouferrache [a], M.A. Ghebouli [b,c], B. Ghebouli [d], M. Fatmi [b,*], H. Bouandas [e], T. Chihi [b], Nouf H. Alotaibi [f], Saikh Mohammad [f], M. Habila [f], M. Sillanpää [g,h]

[a] Department of Physics, Faculty of Sciences, University of Mohamed Boudiaf, M'sila 28000, Algeria
[b] Research Unit on Emerging Materials (RUEM), University Ferhat Abbas of Setif 1, Setif 19000, Algeria
[c] Department of Chemistrys, Faculty of Sciences, University of Mohamed Boudiaf, M'sila 28000, Algeria
[d] Laboratory for the Study of Surfaces and Interfaces of Solid Materials (LESIMS), University Ferhat Abbas of Setif 1, Setif 19000, Algeria
[e] Applied Optics Laboratory, Institute of Optics and Precision Mechanics, University Ferhat Abbas Setif 1, Setif 19000, Algeria
[f] Department of Chemistry, College of Science, King Saud University, P.O. Box 2455, Riyadh 11451, Saudi Arabia
[g] Department of Biological and Chemical Engineering, Aarhus University, Norrebrogade 44, 8000 Aarhus C, Denmark
[h] School of Technology, Woxsen University, Hyderabad, Telangana, India

ARTICLE INFO

Keywords:
Hexafluoromanganets
Thermoelectric materials
Optoelectronic
Ferromagnetic character

ABSTRACT

We analyse a detailed investigation of structure, electronic, optical, magnetic and thermoelectric properties of $(Cs, Rb, K)_2MnF_6$ double perovskites with cubic $Fm\bar{3}m$ space group. The calculation method was the augmented plane-wave functions plus local orbitals as implemented in the WIEN2k code and the GGA followed by the most accurate GGA-mBJ as exchange potentials. The precision of our K_2MnF_6, Rb_2MnF_6 and Cs_2MnF_6 lattice constant compared with their available experimental data is in the range 1.2 % to 3.6 %. The calculated band gap of K_2MnF_6, Rb_2MnF_6 and Cs_2MnF_6 materials advantages them for use in light-emitting diode technology. These materials exhibit ferromagnetic behavior. The negative formation energy, free Helmholtz energy and the dispersion of phonons confirm their thermal, thermodynamic and dynamic stability. The calculated band gap of K_2MnF_6, Rb_2MnF_6 and Cs_2MnF_6 materials advantages them for use in light-emitting diode technology. The p-type charge carriers, direct band gap, and flat conduction and valence bands make them as good thermoelectric materials. The major contribution to the magnetization comes from the unfilled Mn-3d orbital. The high static dielectric constant reduces the recombination rate of charge carriers and the presence of absorption peaks in the ultraviolet region are advantageous in the exploitation in the optoelectronic field. The flat valence and conduction bands, high p-type conductivity, good thermoelectric parameters, as well as non-toxicity make these compounds mainly attractive in the thermoelectric application.

1. Introduction

The study of the properties cited in title allows us to explore the overall performance of A_2MnF_6 (A = Cs, Rb, K) double perovskites. These compounds belong to the cubic $Fm\bar{3}m$ space group in which A take 8e (1/4, 1/4, 1/4) site,Mn has Wyckoff's site 4b (0, 0, 0), while F anion occupy 24a (u, 0, 0) site, where u is a displacement parameter having various value for each compound. Fluorinated materials made of alkali metals are of particular interest in research because they have high luminosity, low cost and good thermal stability. R. Kasa et al. investigated the photoluminescent characteristics in the red emission region of synthesized cubic K_2MnF_6 particles [1]. Researches have been carried out on the infrared and Raman spectra of $K_2MnF_6$and Cs_2MnF_6 obtained in the solid and in solutions of anhydrous HF [2]. We present the reaction for the chemical synthesis of elemental fluorine K_2MnF_6 prepared by the controlled reduction of potassium permanganate in 50 % aqueous hydrofluoric acid [3]:

$$2K_2MnO_4 + 2KF + 10HF + 3H_2O_2 \rightarrow 2K_2MnF_6 + 8H_2O + 3O_2$$

The perovskite materials under study are used in ferroelectric,

* Corresponding author.
E-mail address: fatmimessaoud@yahoo.fr (M. Fatmi).

https://doi.org/10.1016/j.mseb.2024.117550
Received 7 April 2024; Received in revised form 30 May 2024; Accepted 4 July 2024
Available online 14 July 2024

semiconductor, superconductor, catalytic and thermoelectric applications [4–7]. But they have a disadvantage in that their total magnetic moment in the magnetically ordered state is low. There is a class of materials such as complex iron oxides with excellent electronic properties that also show promise for practical applications [8]. Magnetic perovskites possess semi-metallic properties with a high Curie temperature, a quantized magnetic moment and a maximum spin polarizability [9]. The magnetic character of these perovskites is suitable for their use as spin filters, spin valves, magnetic sensors and memory [10,11]. It is reported that the study carried out by Bode shows that Rb_2MnF_6 takes the cubic structure between 70 °C and 100 °C, otherwise the hexagonal shape is preserved. The yellow fluorides K_2MnF_6 with an hexagonal structure, the cubic Rb_2MnF_6 and Cs_2MnF_6 are initially obtained in the form of powders stable in air by fluorination of $AgMn(SO_4)_2$ [12]. K_2MnF_6 is considered a precursor compound of red fluoride-saturated phosphors, which struggle for structural stability. The electronic structure of A_2MnF_6 ($A = Cs, Rb, K$) was characterized using the exchange correlation functionals (WC-GGA), (mBJ) and GGA + U [13]. S.V. Trukhanov et al. studied the cation order–disorder on the crystal structure of other quaternary perovskites (Pr, Nd, Sm, Gd, Tb)$BaMn_2O_{6-\gamma}$, which is tetragonal for $\gamma = 0$ and 1 as well as magnetic state, critical temperature, spontaneous magnetic moment per Mn ion and electrical resistivity [14]. The band gap and absorption coefficient in tetragonal perovskites extracted from the transmission spectra increase with decreasing temperature [15]. The large spontaneous polarization and room temperature multiferroic properties are discovered in doped M−type hexaferrites $SrFe_{12-x}In_xO_{19}$ (x = 0.1; 0.3; 0.6 and 1.2). Thus, the magnetoelectric characteristics of M−type hexaferrites are more advanced than those of the well-known multiferroic $BiFeO_3$ orthoferrite at room temperature [16]. The existence of spontaneous polarization in $SrFe_{12-x}In_xO_{19}$ hexaferrites remains controversial, which is explained by the displacement of Fe ion from the center of an O octahedron in the unit cell [16]. Manganese-doped $Mn_xFe_{3x}O_4$ (x = 0.0, 0.2, 0.6, 0.8) spinel ferrites were produced via co-precipitation using the ethanolamine [17]. M−type $BaFe_{11.9}Al_{0.1}O_{19}$ hexaferrite was successfully synthesized by solid state reactions [8]. Nanocrystalline manganite $La_{0.50}Ba_{0.50}MnO_3$ was synthesized by an optimized sol–gel method [18]. (Pr, Nd, Sm, Eu, Gd, Tb)$BaMn_2O_{6-\gamma}$ compounds have been synthesized by the topotactic reduction–oxidation method [14]. Cs_2TlBiI_6 material cubic double perovskite structure with space group Fm-3 m, direct band gap of 1.37 eV and strong optical absorption in the visible energy range of solar spectrum can be a potential candidate for perovskite based solar cell [19]. $Cs_2AgBiBr_6$ with high light absorption coefficient, good stability can be applied in a variety of photovoltaic devices, such as solar cells, photocatalysis, sensors [20]. The double perovskite material of $Cs_2NaRECl_6$-type, utilizing rare-earth (RE) ions as trivalent element, displays rich optical properties, including visible and infrared light emission through down-shifting, as well as up-conversion emission and radiation-induced emission make it a promising material for optoelectronic devices such as detectors, light-emitting diodes, lasers and energy storage batteries [21].

Our contribution will concentrate on thermal, thermodynamic and dynamic stability through formation energy, Helmholtz free energy and phonon frequencies. We analyse also the detailed investigation of elastic, electronic, optical, magnetic and thermoelectric properties of A_2MnF_6 ($A = Cs, Rb, K$) double perovskites with a cubic structure. The results obtained from the study of these materials show hight static dielectric constant, which reduces the recombination rate of charge carriers and favors their use in optoelectronic devices. The adequate band gap, high static refractive index, ultraviolet energy absorption and power conversion efficiency make them ideal materials for applications in solar cells and thermoelectric field. Perovskite materials show adequate optoelectronic characteristics, so they become a promising solution in the field of photovoltaics. Our goal is to implement nanophotonic concepts to increase the performance of perovskite solar cells.

2. Computational details

The calculation method was the augmented plane-wave functions plus local orbitals as implemented in the WIEN2k code [22] and the GGA followed by the most accurate GGA-mBJ potentials for self-consistency approximations as exchange potential [23]. The GGA-mBJ exchange potential is used in the electronic characterization [24], where the electron–electron correlation effect is treated by the DFT [25]. The plane wave cut-off value ($R_{MT}.K_{max}$), the muffin-tin radii ($R_{M.T}$) of $A(Cs, Rb, K)$ and k-meshes for the Brillouin zone integration as reported in Table 1 ensure perfect convergence. For the calculation of optical and thermoelectric properties, we use k-meshes = 10000, while for elastic constants k = 5000 is sufficient. The maximum radial expansion $I_{max} = 10$ au^{-1} expresses the charge density and potential. The cut-off energy that separates valence and core states was − 8 Ry and 10^{-3} e was used as charge convergence. Valence electrons participate in the formation of chemical bonding, while core electrons influence the chemical reactivity of an atom. The electronic configuration is noticed as Cs: [Xe] 6 s^1, Rb: [Kr] 5 s^1, K: [Ar] 4 s^1, Mn: [Ar] $3d^5$ 4 s^2 and F: [He] 2 s^2, $2p^5$. R_{MT} influences the electronic characteristics, but its effect is not significant compared to that of GGA-mBJ exchange potential. The formation energy translates the binding force of a solid, and it is the energy needed to dispatch the solid into isolated atoms when all the bonds are broken. We take note that GGA-mBJ corrects the formation energy, transition energy level, lattice constant, electrostatic potential, valence band maximum and total energy.

3. Results and discussions

3.1. Structural characterization and stability

A_2MnF_6($A = Cs, Rb, K$) take the cubic crystal structure with space group $Fm\bar{3}m(No:225)$. The crystal structure is depicted in Fig. 1. *Mn* atoms are located at the octahedral center 4a (0; 0; 0),*F* atoms occupy the corners (0; 0; u = 0.2296) and *A* atoms are in the spaces between the octahedrons 8c (1/4; 1/4; 1/4). The structural study is characterized by volume optimization, where the energy of the unit cell is minimized with respect to the volume and adjusted by the Birch-Murnaghan equation of state. For a stable specific volume, whose energy reaches a minimum value called fundamental energy, the lattice constant, bulk modulus and its pressure derivative, ground state energy and formation energy are shown in Table. 2. The lattice constant accuracy of the cubic K_2MnF_6, Rb_2MnF_6 and Cs_2MnF_6 according to their available experimental data are estimated between (1.2 to 3.6) % [26]. The bulk modulus values of cubic K_2MnF_6, Rb_2MnF_6 and Cs_2MnF_6 agree well with those reported using the semi-empirical model [27], where the error is in the range (2.6 to 6.6) %. The pressure derivative of bulk modulus and minimum energy of $A(Cs, Rb, K)_2MnF_6$ are in good concordance with those reported in reference [13]. The formation energy translates the binding force of a solid, and it is the energy needed to dispatch the solid into isolated atoms when all the bonds are broken. The negativity of the formation energy of a material reflects its thermal stability.

$$E_{form}^{A_2MnF_6} = E_{tot}^{A_2MnF_6} - \frac{E_{tot}^{A}}{2} - E_{tot}^{Mn} - \frac{E_{tot}^{F}}{6} \quad (1)$$

Helmholtz free energy were calculated with harmonic approximation as a function of temperature as shown in Fig. 2. The negative value

Table 1
The values of R_{MT}xKmax, R_{MT} of each constituent and k-point of A_2MnF_6 ($A = Cs, Rb, K$) using GGA.

Type-I	R_{MT}xKmax	R_{MT} (A)	R_{MT} (Mn)	R_{MT} (F)	k-point
Cs_2MnF_6	9	2.50	1.82	1.64	1000
K_2MnF_6	9	2.50	1.68	1.52	1000
Rb_2MnF_6	9	2.50	1.81	1.64	1000

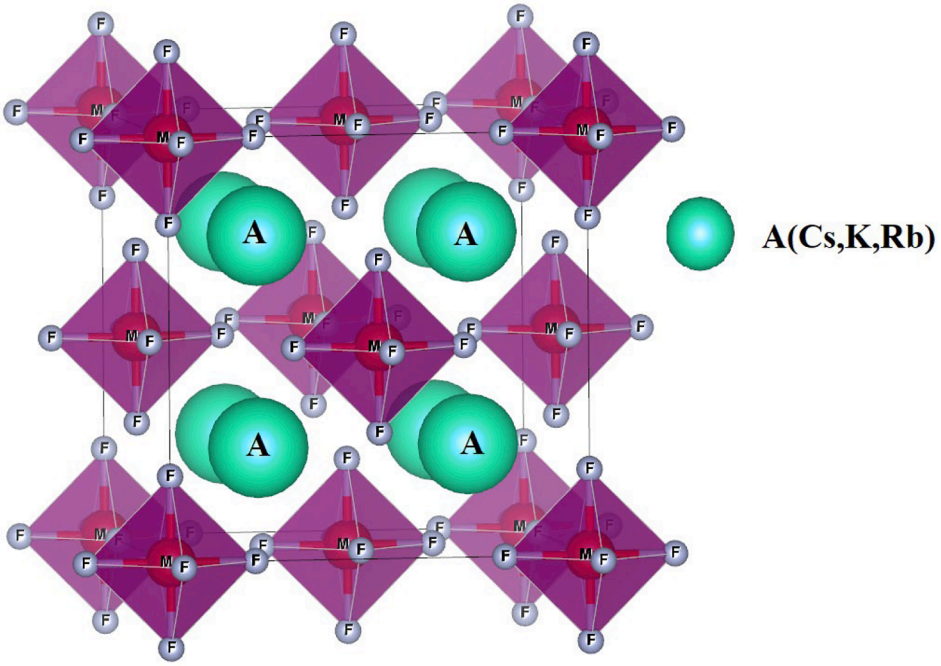

Fig. 1. Schematic representation of A_2MnF_6 (A = Cs, Rb, K) structure.

Table 2
Lattice constant (a_0), bulk modulus (B) and its pressure derivative (B′), minimum energy (E_0) and formation energy E_{foma} of A_2MnF_6 (A = Cs, Rb, K).

	a_0 (Å)	B (GPa)	B′	E_0 (Ry)	$E_{fom.}$ (eV)
Cs_2MnF_6	9.10	51.22	5.356	−34677.98295	−4.37
	8.972 [26]	52.71 [27]	5.00 [13]	−34678.003 [13]	
	9.033 [13]	51.87 [13]			
K_2MnF_6	8.3247	66.85	3.859	−5925.333698	−4.49
	8.22 [26]	71.31 [27]	5.0 [13]	−5921.672 [13]	
Rb_2MnF_6	8.656	64.42	2.96	−15442.759270	−4.52
	8.528 [26]	62.74 [27]	5.00		

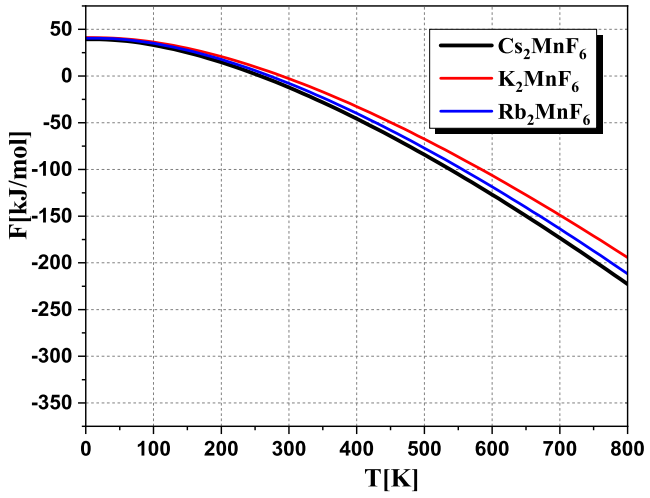

Fig. 2. Helmholtz free energy as a function of temperature for A_2MnF_6 (A = Cs, Rb, K).

and the decrease of Helmholtz free energy when the temperature is enhanced for all double perovskites indicate the thermodynamic stability of these double perovskites. This stability is more pronounced in the sequence $Cs \rightarrow Rb \rightarrow K$. We display in Fig. 3 the phonon dispersion diagrams along some of the high symmetry lines of their corresponding Brillouin zones and total densities of states for A_2MnF_6 (A = Cs, Rb, K) double perovskites using GGA-mBJ functional. Rb_2MnF_6 and Cs_2MnF_6 show no imaginary phonon modes throughout the Brillouin zone (all frequencies are positive) confirming their dynamical stability. While K_2MnF_6 has one line with negative frequencies, but it has a tendency to dynamical stability.

3.2. Elastic constants and mechanical characteristics

The elastic constants are calculated by the nonlinear using the Charpin method [28]. $A(Cs, Rb, K)_2MnF_6$ double perovskites with cubic symmetry have three parameters C_{11}, C_{12} and C_{44} as reported in Table 3, along with their mechanical characteristics estimated through these constants. The shear modulus, bulk modulus, anisotropy factor, Young's modulus, Poisson's and B_H/G_H ratios for A_2MnF_6 (A = Cs, Rb, K) as well as their Voigt and Reuss limits are reported in Table 3. Elastic constants and bulk modulus satisfy the stability criteria $C_{11}+2C_{12}\rangle 0, C_{44}\rangle 0, C_{11}-C_{12}\rangle 0, C_{12}\langle B\langle C_{11}$ and therefore these double perovskites are mechanically stable. Elastic moduli of these double perovskites being very low, this leads to their easy deformation and less resistance to stretching or bending. Shear and bulk moduli, as well as their Voigt and Reuss limits of K_2MnF_6 and Rb_2MnF_6, are higher than those of Cs_2MnF_6, which indicates that K_2MnF_6, and Rb_2MnF_6 are harder and stiffer compared with Cs_2MnF_6. Also, young's modulus confirms the larger resistance to uniaxial deformation of Cs_2MnF_6 and Rb_2MnF_6. We note that the bulk modulus is located between shear modulus and Young's modulus for K_2MnF_6 and Rb_2MnF_6, signifying that these two compounds allow uniaxial deformation more easily than volumetric deformation. A high B/G ratio is associated with ductility, whereas a low value corresponds to the brittleness. The critical value separating ductile and brittle material is 1.75.Cs_2MnF_6 and K_2MnF_6 are ductile, while Rb_2MnF_6 is brittle. The values of Poisson's ratio $\nu > 0.25$ support forces as central type in all compounds. According to condition for anisotropy, all studied double perovskites are anisotropic and the anisotropy is more

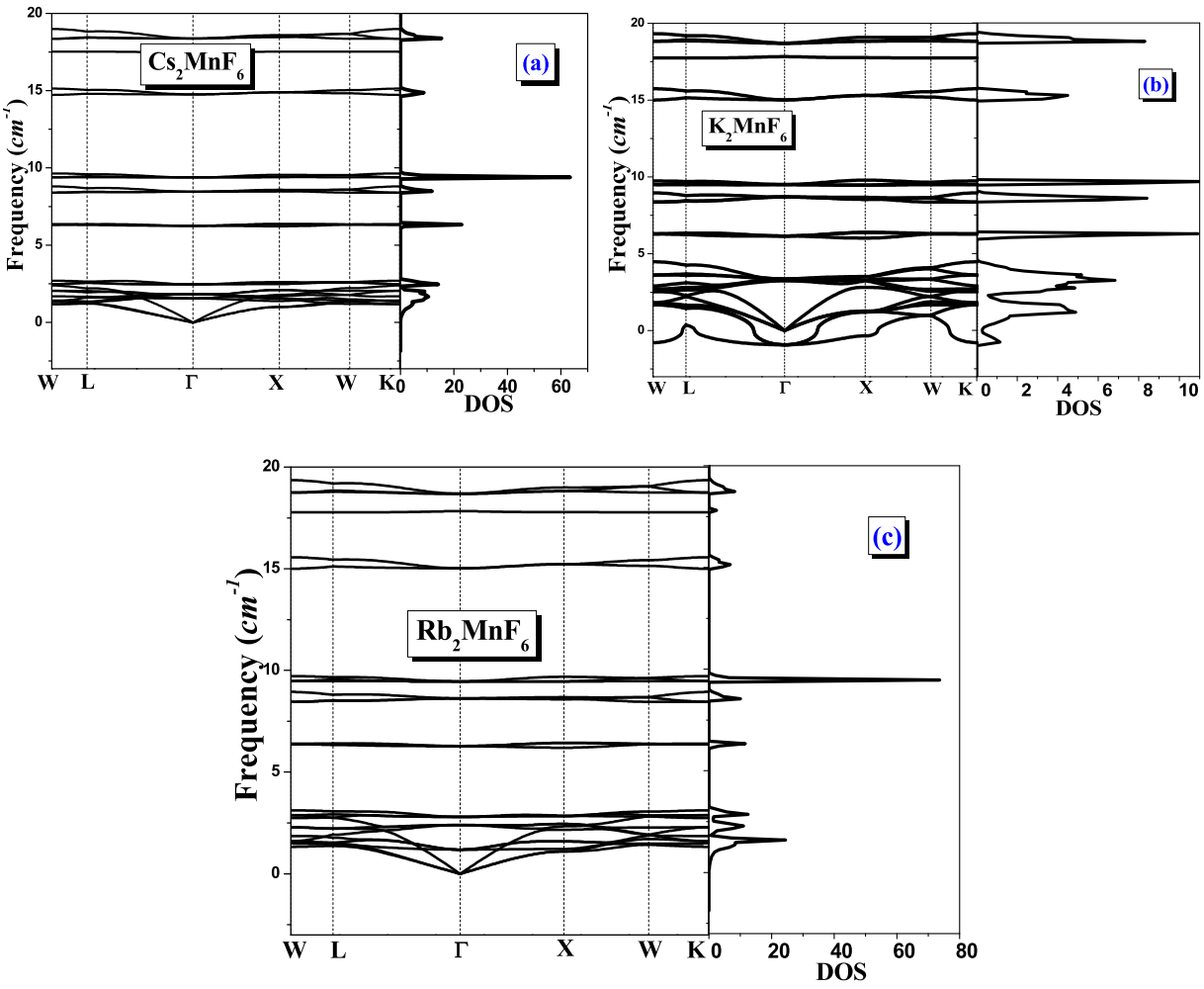

Fig. 3. Phonon band structures and DOS of A_2MnF_6 (A = Cs, Rb, K) using GGA-mBJ.

Table 3
Elastic constants, shear modulus, bulk modulus, anisotropy factor, Young's modulus, Poisson's coefficient and B_H/G_H ratio for A_2MnF_6 (A = Cs, Rb, K).

	Cs_2MnF_6	K_2MnF_6	Rb_2MnF_6
C_{11} (GPa)	75.76	135.45	157.65
C_{12} (GPa)	37.35	50.33	32.53
C_{44} (GPa)	17.27	40.42	33.41
G_v (GPa)	18.04	41.27	45.07
G_R (GPa)	17.99	41.25	41.06
G_H (GPa)	18.02	41.26	43.06
B_H (GPa)	50.15	78.70	74.24
A	0.89	0.94	0.53
E_V (GPa)	48.33	105.40	112.45
E_R (GPa)	48.21	105.35	104.02
E_H (GPa)	48.27	105.38	108.27
ν_V	0.33	0.27	0.24
ν_R	0.33	0.27	0.26
ν_H	0.33	0.27	0.25
B_H/G_H	2.78	1.90	1.72

pronounced in Rb_2MnF_6. Figs. 4-6 show 3D surface of Young's modulus, bulk modulus and Poisson's ratio of K_2MnF_6, Rb_2MnF_6 and Cs_2MnF_6 double perovskites. It is presented by a contour along each graph in different directions using GGA-mBJ functional. We note that all parameters are isotropic, except Poisson's ratio and Young's modulus of Rb_2MnF_6 and Cs_2MnF_6 are anisotropic.

3.3. Electronic band structures

The band structure plots for A_2MnF_6 (A = Cs, Rb, K) compounds in both spin directions using mBJ-GGA are presented in Fig. 7. The valence band maximum and the conduction band minimum lie at the Γ symmetry point, suggesting a direct band gap nature. The band gap in terms of the spin-resolved band structure using GGA and mBJ-GGA are reported in Table 4. Semiconductors $A(Cs, Rb, K)_2MnF_6$ have flat conduction and valence bands in both spins. The wide band gap character in spin dn mode is observed, this difference between the majority and minority spins is due to the hybridization of the $Mn-3d$ and $F-2p$ states. The GGA calculation underestimates the band gap, then we use the mBJ-GGA in order to predict the correct band gap. The density of states plots, as shown in Fig. 8 explain the contribution of different atomic states to the band structure for A_2MnF_6 (A = Cs, Rb, K). The partial density of states calculations of the selected double perovskites with spin polarized indicate that the major contribution to the TDOS is due to the $K-3p$,$Rb-4d$,$Cs-4p$,$Mn-3d$ and $F-2p$ sites. The band centered in the upper valence band is mainly due to $F-2p$ site with a minor contribution from $Mn-3d$ state in both spin directions. The lower conduction band is empty and the first occupied conduction band is due to $F-2p$ and $Mn-3d$. The electronic band structure and density of states show that all studied double perovskites exhibit semiconductor character in spin up and spin down direction. While, Cs_2MnF_6 is half metallic, exhibiting semiconductivity in spin up direction and metallic behavior in spin down direction [29,30]. The zero value of the state density explains that the materials under study are semiconductors. The

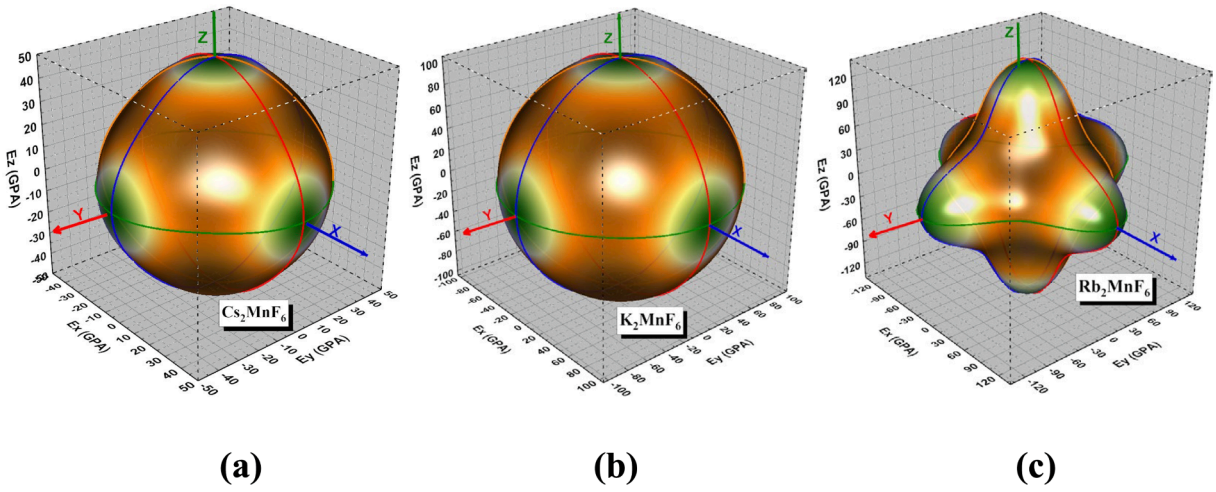

Fig. 4. 3D surface of the Young's modulus for (a) Cs_2MnF_6, (b) K_2MnF_6, (c) Rb_2MnF_6.

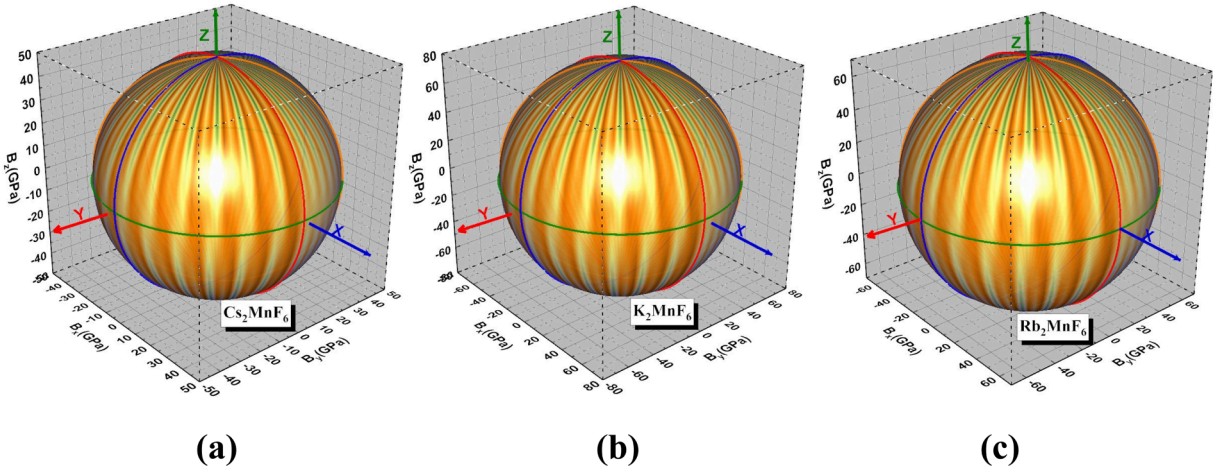

Fig. 5. 3D surface of the Bulk modulus for (a)Cs_2MnF_6, (b) K_2MnF_6, (c)Rb_2MnF_6.

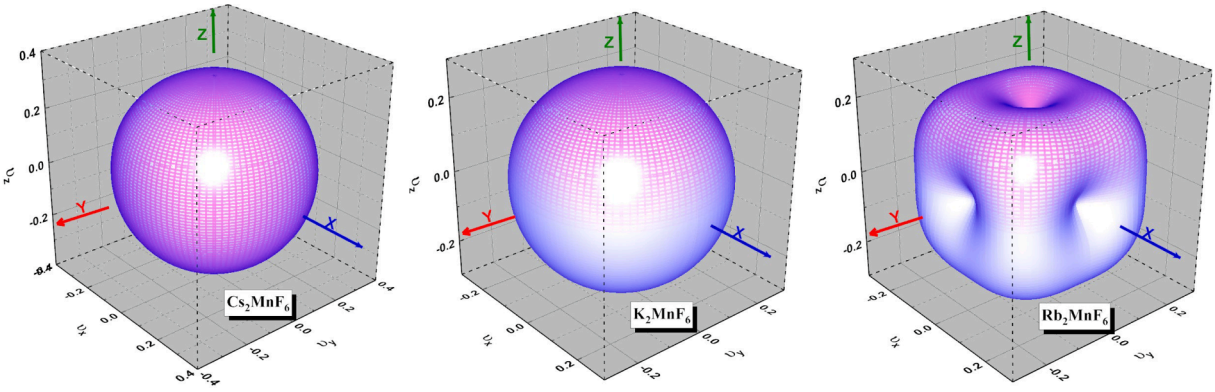

Fig. 6. 3D surface of the Poisson's coefficient for (a) Cs_2MnF_6, (b) K_2MnF_6, (c) Rb_2MnF_6.

wide band gap observed in these double perovskites suggest their use as excellent materials for light emitting diode technology. Cs_2TlBiI_6 material cubic double perovskite structure with space group Fm-3 m, direct band gap of 1.37 eV and strong optical absorption in the visible energy range of solar spectrum can be a potential candidate for perovskite based solar cell [19].

3.4. Optical properties

Fig. 9 summarizes the plots of real (a) and imaginary (b) parts of the dielectric function, refractive index (c), extinction coefficient (d), energy loss (e), absorption coefficient (f), reflectivity (g) and optical conductivity (h) of A_2MnF_6 ($A = Cs, Rb, K$) as a function of photon energy using GGA-mBJ. The real part explains the electronic polarizability, while the imaginary part informs us about absorption. The static dielectric

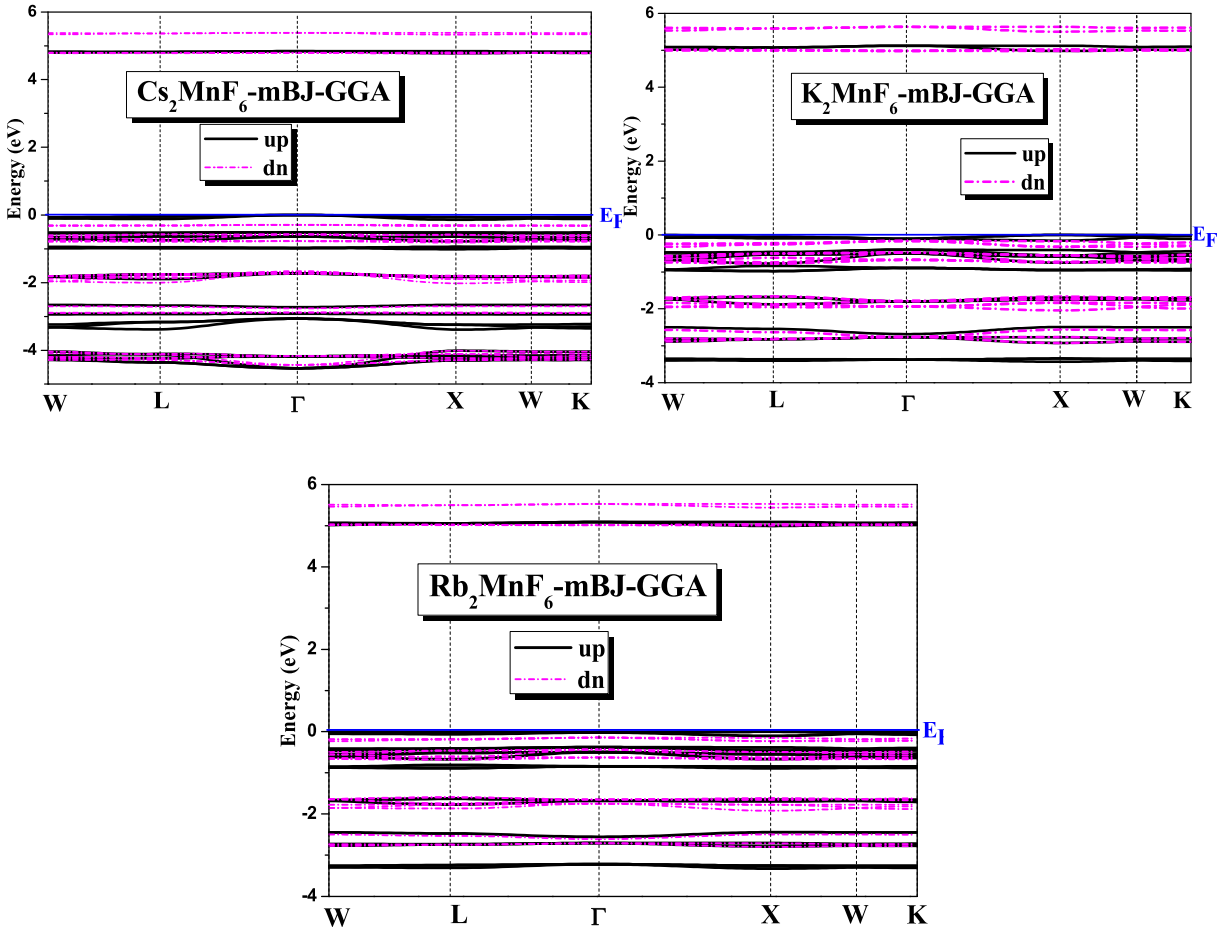

Fig. 7. The electronic band structure spin up and dn A_2MnF_6 *(A = Cs, Rb, K)* using mBJ-GGA.

Table 4
Band gap of A_2MnF_6 *(A = Cs, Rb, K)* using GGA and mBJ-GGA.

	GGA		GGA-mBJ	
	up	Dn	up	dn
Cs_2MnF_6	2.717	3.818	4.783	5.064
	2.79 [13]		6.34 [13]	
K_2MnF_6	2.685	3.752	4.978	5.138
	2.79 [13]	3.85 [13]	5.26 [13]	5.42 [13]
Rb_2MnF_6	2.72	3.78	4.997	5.145
	2.4 [13]	3.5 [13]	5.13 [13]	5.36 [13]

constant is 2, 2.2 and 3.1 for K_2MnF_6, $Cs_2MnF_6$and Rb_2MnF_6. The real part becomes negative for an energy 12 eV, 22 eV and 25 eV for Cs_2MnF_6, $Rb_2MnF_6$and K_2MnF_6.The dielectric function process an excited field who opposes to the external field with lower frequency. The high value of the static dielectric constant reduces the recombination rate of charge carriers and the presence of peaks in the ultraviolet region indicate that these materials are used in the optoelectronic field. The imaginary part of the dielectric function is connected to the absorption inside the material. The critical point of the imaginary part called energy threshold designates the band gap due to the electronic transition between the valence band and the conduction band in the GGA-mBJ approximation for both spins. The refractive index gives information on the amount of light refracted by a material. The static refractive index is 1.25, 1.35 and 1.85 for K_2MnF_6, Cs_2MnF_6 and Rb_2MnF_6. It reaches a maximum value in the extreme ultraviolet region 2.16, 2.12, 3.7 and 2.6 and decreases up to where it reaches the unity value. The real part shape of the dielectric constant is identical to that of the refractive index. The refractive index has an inverse relation with band gap. The extinction coefficient starts at the threshold energy. Cs_2MnF_6, K_2MnF_6 and Rb_2MnF_6have a maximum of extinction coefficient 1.5, 2 and 5.5, and it decreases until it disappears. The extinction coefficient and the imaginary part of dielectric function have a similar appearance. There is no loss for energy below the band gap. The maximum loss are 0.8 %, 1.5 % and 3.5 % for Rb_2MnF_6, Cs_2MnF_6 and K_2MnF_6, therefore, losses are negligible. The first absorption region in the ultraviolet energy range was observed from 5 eV to 10 eV for A_2MnF_6 *(A = Cs, Rb, K)*. The light absorption threshold is 5.064 eV, 5.138 eV and 5.145 eV in spin dn and 4.783 eV, 4.978 eV and 4.997 eV in spin up for Cs_2MnF_6, K_2MnF_6 and Rb_2MnF_6 using GGA-mBJ. Peaks existing in the absorption spectra correspond to the electronic transitions from bonding states to the antibonding states. $Cs_2AgBiBr_6$ with its high light absorption coefficient, good stability can be applied in a variety of photovoltaic devices, such as solar cells, photocatalysis, sensors [20]. The static reflectivity values are 0.02 %, 0.03 % and 0.1 for K_2MnF_6,Cs_2MnF_6 and Rb_2MnF_6. The reflectivity spectra have two parts, the first one in the range 0 to 5 eV, where the variation is almost constant, the second in the range 5 to 30 eV, where the reflectivity passes through a set of maximum and minimum. High dielectric constant and optical absorption of the double perovskites under study make them perform better in solar cells. Optical conductivity shows the transportation of electrons in the present of electromagnetic radiations. The maximum peaks of σ(ω) for A_2MnF_6 *(A = Cs, Rb, K)* occur in ultra-violet region of photon spectra. The double perovskite material of $Cs_2NaRECl_6$-type, utilizing rare-earth (RE) ions as trivalent element, displays rich optical properties, including visible and infrared light emission through down-shifting, as well as up-conversion emission and radiation-induced emission make it a promising material

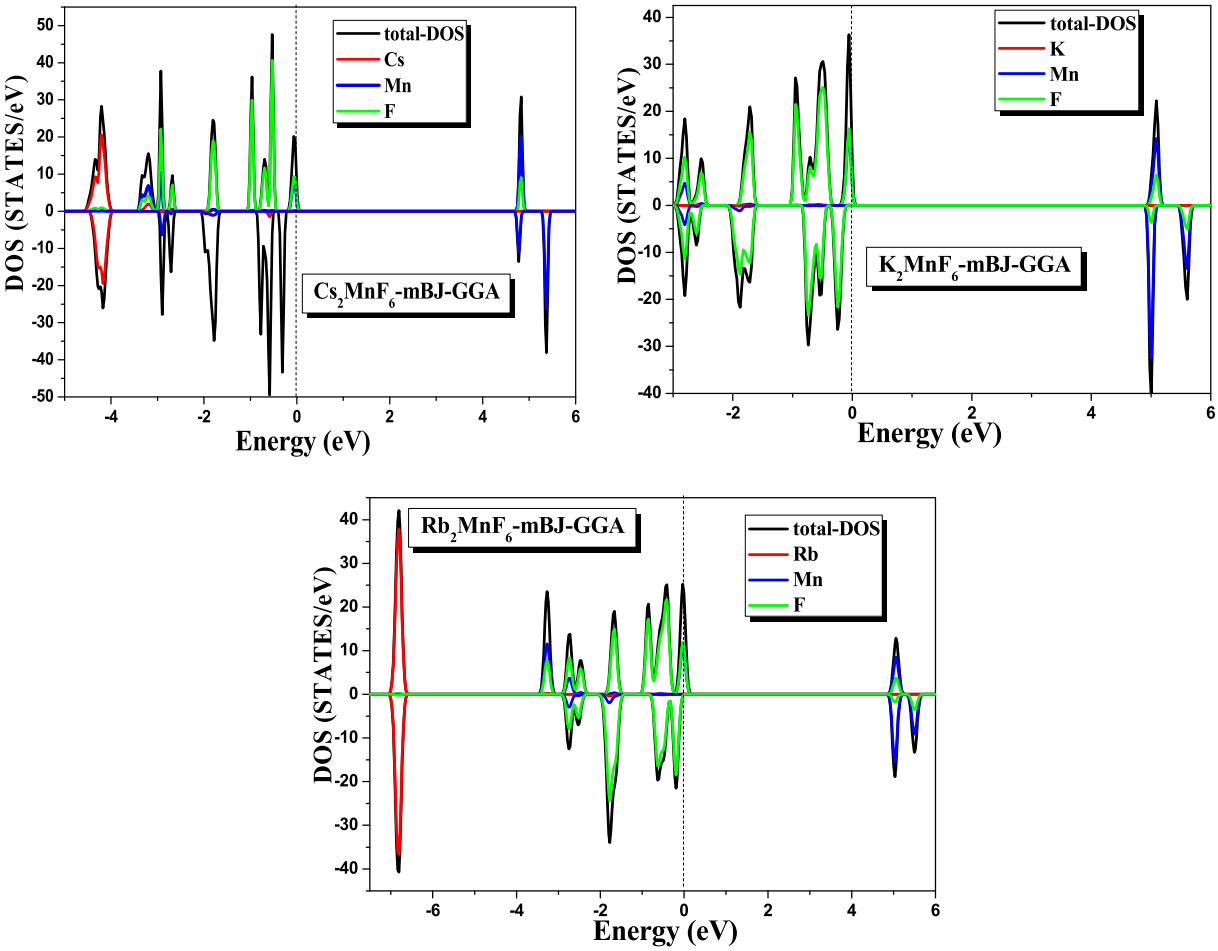

Fig. 8. The density of states of A_2MnF_6 (A = *Cs, Rb, K*) computed by mBJ-GGA.

for optoelectronic devices such as detectors, light-emitting diodes, lasers and energy storage batteries [21].

3.5. Magnetic properties

We have performed the spin polarized DFT calculations with GGA and mBJ-GGA approximations in the study of magnetic properties for A_2MnF_6 (A = *Cs, Rb, K*). The calculation of the magnetic moment is used in determining the magnetic nature of these double perovskites. These compounds exhebit ferromagnetic character with major contribution to the magnetization comes from the unfilled Mn-3d orbital. The calculated interstitial, atomic and total magnetic moment for $A(Cs, Rb, K)_2MnF_6$ are reported in Table 5 using GGA and mBJ-GGA. We notice that both approaches give the same total magnetic moment. The partial magnetic moments and the interstitial magnetic moment have the same direction, which explain the ferromagnetic comportment. Magnetic calculations reveal strong ferromagnetic nature of these compounds [29,30]. A_2MnF_6 (A = *Cs, Rb, K*) double perovskites have an integer magnetic moment according to the Slater-Pauling rule. The partial magnetic moments in the interstitial region have the same direction. Stoichiometry is an important factor in complex oxides. The deviation in the concentration of the original cations modifies the charge state of the transition metal cations, hence the modification of the magnetic and electrical parameters [31]. Vacancies in 3D metals lead to the formation of a weak magnetic state, change their charge state, which affect magnetic and electrical parameters such as total magnetic moment, Curie point, conductivity and the band gap [32]. A spin glass is a magnetic state of a substance having particular properties. The most important is the divergence between the relative orientation of magnetic moments and their exchange interactions. The condition for the formation of a spin glass cluster occurs when there is a random distribution of values and signs of exchange interactions. For a classical spin glass, the external magnetic field causes a transition to a ferromagnetic state and changes the divergence temperature of the Zero Field Cooling (ZFC) and Field Cooling (FC) of the specific magnetic moment according to the power law $T = a + bH^n$ [33,32]. This criterion determines the nature and mechanism of the formation of an inhomogeneous magnetic state [34]. Structural separation into two phases occurs with strong competition of the ferro and anti ferromagnetic interactions between Mn magnetic moments. As a result, there is a new magnetic state, where a cluster spin glass is reflected in the magnetic ordering and the freezing of magnetic moments. The increase in the average crystallite size causes a non-monotonic increase in the Curie point and in the spontaneous magnetic moment [35,18]. It is reported that ferrite content significantly affects magnetoelectric behaviour [35]. The anomalous behavior of the magnetic properties is explained by the competition between two size effects, namely, the frustration of the indirect exchange interactions and the crystal lattice [18]. At zero external field, the magnetic state is a cluster spin glass, which results from frustration exchange interactions. An increase in external magnetic field leads to fragmentation of ferromagnetic clusters and then to an increase in the degree of polarization of local spins of manganese and the emergence of long-range ferromagnetic order [36]. The stability of the spin glass under pressure is associated with restrictions on the maximum possible size of ferromagnetic clusters in the presence of vacancies [37]. The formation of the spin glass is due to competition between ferromagnetic double exchange interaction and antiferromagnetic superexchange interaction, enhanced by positional disorder in the sublattice [37].

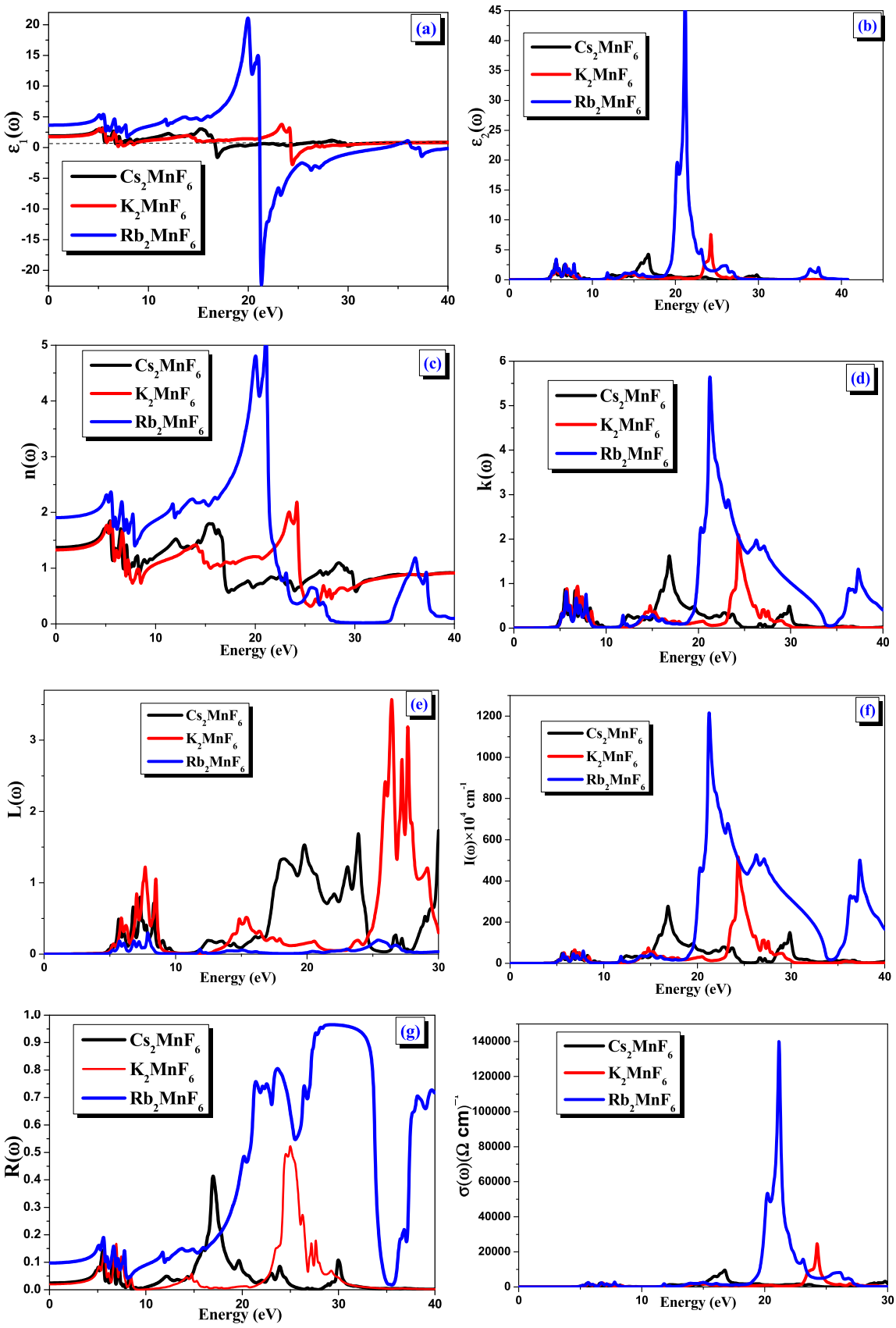

Fig. 9. The real (a) and imaginary (b) parts of the dielectric function, refractive index (c), extinction coefficient (d), energy loss (e), absorption coefficient (f), reflectivity (g), optical conductivity (h) as a function of photon energy energy for A_2MnF_6 *(A = Cs, Rb, K)* double perovskites using mBJ- GGA.

Table 5
Calculated interstitial, atomic magnetic moment and total atomic magnetic moment for A_2MnF_6 ($A = Cs, Rb, K$).

	Approximation	$m_{interstitial}$/at. (μ_B)	m_A/at. (μ_B)	m_{Mn}/at. (μ_B)	m_F/at. (μ_B)	m_{total} (μ_B)
Cs_2MnF_6	GGA	0.21839	0.00206	2.57812	0.03323	3.00 3.00 [13]
	GGA-mBJ	0.11160	0.00274	2.65278	0.03836	3.00
K_2MnF_6	GGA	0.31988	0.00127	2.48484	0.03217	3.00 3.00 [13]
	GGA-mBJ	0.17719	−0.00021	2.59022	0.03884	3.00
Rb_2MnF_6	GGA	0.22107	0.00145	2.57594	0.03334	2.99998 3.0 [13]
	GGA-mBJ	0.09501	0.00022	2.65278	0.04196	3.00

3.6. Thermoelectric characteristics

Seebeck coefficient, electrical conductivity, thermal conductivity and figure of merit are calculated by Boltzmann transport theory with BoltzTraP code in mBJ-GGA with spin-up and spin-dn. The results of the thermoelectric parameters as a function of temperature relating to the semiconductors A_2MnF_6 ($A = Cs, Rb, K$) are depicted in Figs. 10 and 11. The temperature range is chosen 0 to 1000 K. The Seebeck values of A_2MnF_6 ($A = Cs, Rb, K$) are positive throughout this temperature range for both spins, therefore the conductivity comes from p-type charge carriers. The Seebeck value decreases with increasing temperature in all studied perovskites, but in the temperature range 100 K to 1000 K, its effect is not harmful and especially in the case of the Rb_2MnF_6 compound. Seebeck coefficient traduces thermoelectric performance of materials and describes the ratio of voltage difference to that of temperature difference computed under linear response regime. Higher magnitudes are resulted in the sequences $K_2MnF_6 \rightarrow Cs_2MnF_6 \rightarrow Rb_2MnF_6$, High values of Seebeck are obtained in the case of spin-dn. At room temperature, the Seebeck of K_2MnF_6, Cs_2MnF_6 and Rb_2MnF_6 is 1800 μVK^{-1}, 1000 μVK^{-1} and 600 μVK^{-1} (185 μVK^{-1}, 175 μVK^{-1} and 125 μVK^{-1}) for spin-dn (spin-up). The σ is related to carrier concentration by the relation $\sigma = ne\mu$, where μ, e and n are the mobility, electronic charge and carrier concentration of compounds. The electrical conductivity σ increases up to room temperature, then it decreases continuously in the case of spin-up. The maximum electrical conductivity observed is 4×10^4 $(\Omega ms)^{-1}$, 3×10^4 $(\Omega ms)^{-1}$ and 2.2×10^4 $(\Omega ms)^{-1}$ for K_2MnF_6, Cs_2MnF_6 and Rb_2MnF_6. We report room temperature values of σ as 2.2×10^4 $(\Omega ms)^{-1}$, 2.7×10^4 $(\Omega ms)^{-1}$ and 3.5×10^4 $(\Omega ms)^{-1}$ for Rb_2MnF_6, Cs_2MnF_6 and K_2MnF_6. For the spin-dn, the electrical conductivity increases continuously with increasing temperature for Rb_2MnF_6 and is practically zero for Cs_2MnF_6 and K_2MnF_6. The thermal conductivity of a material is due to the electronic (k_{el}) and phonons (k_{ph}) contributions. In accordance with the BoltzTraP code, we ignore the contribution of phonons (k_{ph}) and only consider the electronic part (k_{el}) of the thermal

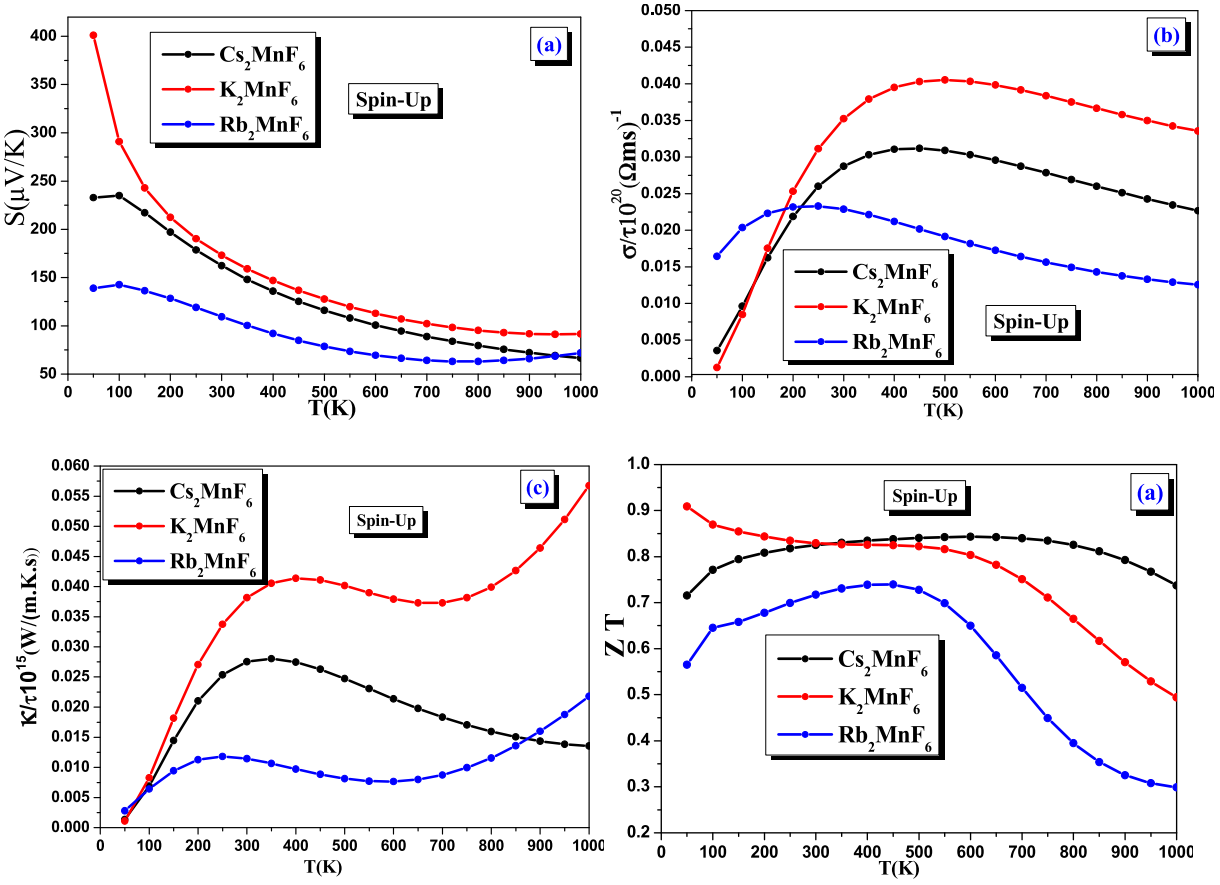

Fig. 10. Effect of temperature on (a) Seebeck, (b) electrical conductivity, (c) thermal conductivity and (d) figure of merit ZT for A_2MnF_6 ($A = Cs, Rb, K$) within mBJ-GGA approximation and Spin-up.

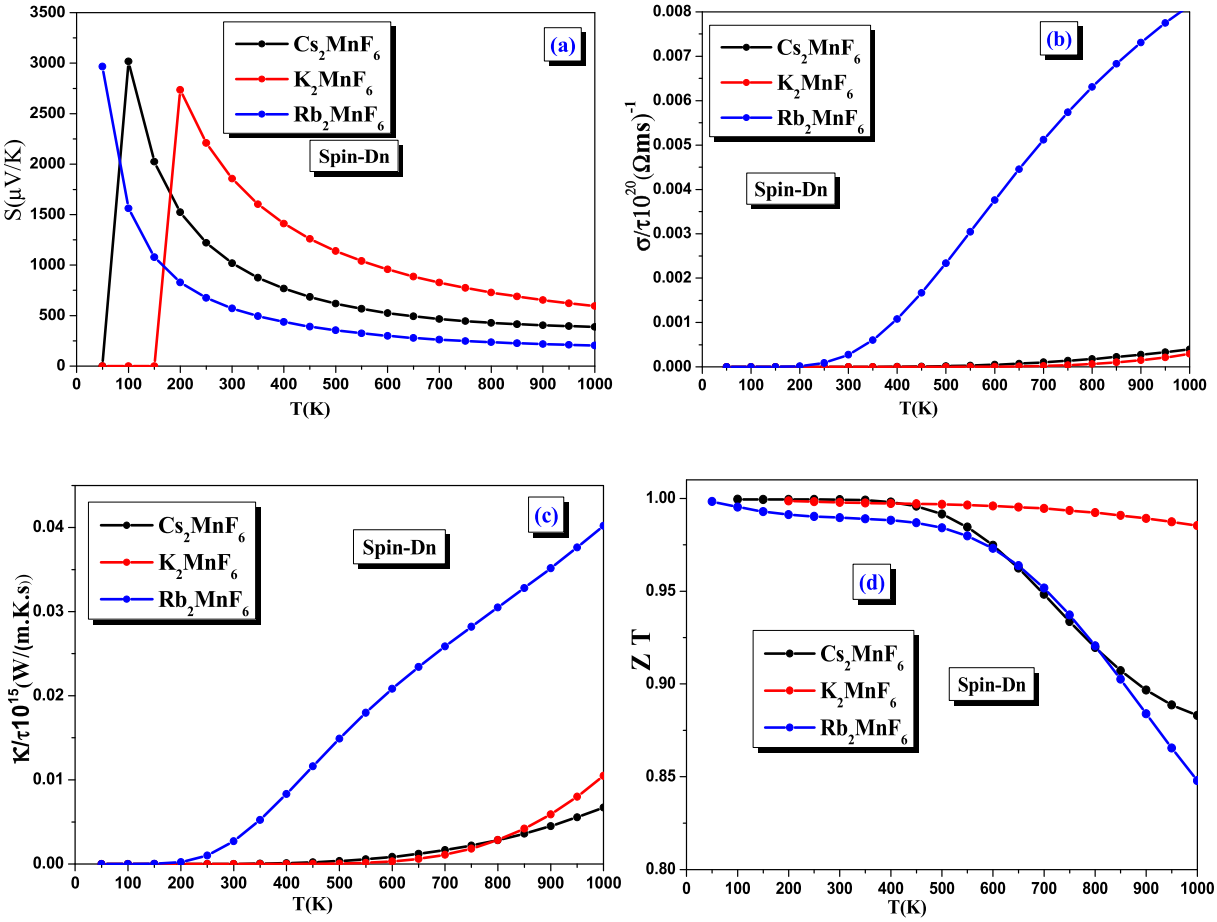

Fig. 11. Effect of temperature on (a) Seebeck, (b) electronic thermal conductivity, (c) total thermal conductivity, (d) figure of merit of A_2MnF_6 *(A = Cs, Rb, K)* within the mBJ-GGA approximation for Spin-dn.

conductivity. In the case of spin-up, the electronic conductivity increases until room temperature, then keeps a practically constant value up to 700 K for Rb_2MnF_6 and K_2MnF_6 then increases again. Whereas for Cs_2MnF_6, it decreases beyond the room temperature. For the spin-dn, the electronic conductivity appears at 200 K for Rb_2MnF_6 and 400 K for K_2MnF_6 and Cs_2MnF_6 respectively and then increases continuously, with a weaker increase for K_2MnF_6 and Cs_2MnF_6. The efficiency of the transport properties of semiconductors is characterized by a dimensionless quantity which is the figure of merit *ZT*. Its mathematical expression is $ZT = \frac{S^2\sigma T}{k}$, where *S*,$\sigma$,*T* and *k* are Seebeck, electrical conductivity, absolute temperature and thermal conductivity of material, which is due to the electronic (k_{el}) and phonons (k_{ph}) contributions. A high value of ZT requires high values of S, σ and T and a minimum thermal conductivity k. The contribution of phonons (k_{ph}) to thermal conductivity is unknown. The figure of merit of K_2MnF_6 is close to unity and unaffected by temperature, while for Rb_2MnF_6 and Cs_2MnF_6 it is reduced to nearly o.90 at high temperature.

4. Conclusion

We performed ab initio calculations within the mBJ-GGA approximation for finding new materials with preferred elastic, electronic, optical, magnetic and thermoelectric characteristics. Structural stability of A_2MnF_6 *(A = Cs, Rb, K)* was confirmed from computed formation energy, Helmholtz free energy and phonon dispersion diagrams. The calculated lattice constant and bulk modulus are consistent with their experimental results. The spin polarized band structure and density of states indicate that all studied double perovskites have wide band gap in both spin configurations. Semiconductors A_2MnF_6 *(A = Cs, Rb, K)* have flat conduction and valence bands in both spins. A_2MnF_6 *(A = Cs, Rb, K)* double perovskites have an integer magnetic moment according to the Slater-Pauling rule. Electronic band structures and density of states show that these semiconducturs are p-type carriers. The calculated thermal conductivity of Cs_2MnF_6 and Rb_2MnF_6 is sufficiently low to allow the compounds under study to have a good electrical conductivity. The figure of merit of the three compounds calculated at high temperatures, the flat valence and conduction bands, high p-type conductivity, high Seebeck and ZT, as well as non-toxicity make these compounds mainly attractive in the thermoelectric application. Our hope is that the results obtained in this work serve as a reference for future projects on the compounds under study.

CRediT authorship contribution statement

K. Bouferrache: Methodology, Investigation. **M.A. Ghebouli:** Funding acquisition, Data curation. **B. Ghebouli:** Funding acquisition, Data curation. **M. Fatmi:** Supervision. **H. Bouandas:** Investigation. **T. Chihi:** Supervision, Software. **Nouf H. Alotaibi:** Methodology, Funding acquisition. **Saikh Mohammad:** Software, Resources. **M. Habila:** Supervision. **M. Sillanpää:** Supervision.

Declaration of competing interest

The authors declare that they have no known competing financial interests or personal relationships that could have appeared to influence the work reported in this paper.

Data availability

The authors do not have permission to share data.

Acknowledgements

This Work Was Funded by The Researchers Supporting Project Number (RSPD2024R551), King Saud University, Riyadh, Saudi Arabia.

References

[1] R. Kasa, Y. Arai, T. Takahashi, S. Adachi, J. Appl. Phys. 108 (11) (2010) 113503.
[2] L.B. Asprey, M.J. Reisfeld, N.A. Matwiyoff, J. Mol. Spectrosc. 34 (3) (1970) 361.
[3] H. Bode, H. Jenssen, F. Bandte, Angew. Chem. 65 (11) (1953) 304.
[4] R. Ullah, M.A. Ali, S. Murad, A. Khan, S.A. Dar, I. Mahmood, A. Laref, Mater. Res. Express 6 (2019) 125901.
[5] I. Khan, N. Shehzad, I. Ahmad, Z. Ali, S. Jalali-Asadabadi, Int. J. Mod. Phys. B 31 (2017) 1750148.
[6] N. Erum, M.A. Iqbal, Commun. Theor. Phys. 66 (2016) 571.
[7] M.H. Benkabou, M. Harmel, A. Haddou, A. Yakoubi, N. Baki, R. Ahmed, Y. Al-Douri, S.V. Syrotyuk, H. Khachai, R. Khenata, C.H. Voon, M.R. Johan, Chin. J. Phys. 56 (2018) 131–144.
[8] A.V. Trukhanov, S.V. Trukhanov, L.V. Panina, V.G. Kostishyn, I.S. Kazakevich, A. V. Trukhanov, E.L. Trukhanov, V.O. Natarov, V.A. Turchenko, M.M. Salem, A. M. Balagurov, J. Magn. Magn. Mater. 426 (2017) 487–496.
[9] L. Li, Q. Gao, G. Lei, H.H. Xie, J.B. Deng, X.R. Hu, J. Phys. Chem. Solids 94 (2016).
[10] R. Ullah, M.A. Ali, G. Murtaza, A. Khan, A. Mahmood, Int. J. Energy Res. 44 (2020) 9035–9049.
[11] A. Hirohata, K. Takanashi, J. Phys. D 47 (2014) 193001.
[12] R. Hoppe, K.H. Wandner, J. Fluorine Chem. 23 (1983) 589–592.
[13] M. Faizan, S.H. Khan, A. Khan, A. Laref, G. Murtaza, Int. J. Modern Phys. B 32 (24) (2018) 1850270, https://doi.org/10.1142/S0217979218502703.
[14] S.V. Trukhanov, I.O. Troyanchuk, M. Hervieu, H. Szymczak, K. Bärner, Phys. Rev. B 66 (2002) 184424, https://doi.org/10.1103/physrevb.66.184424.
[15] I.V. Bodnar, V.V. Khoroshko, V.A. Yashchuk, V.F. Gremenok, M. Kazi, M. U. Khandaker, T.I. Zubar, D.I. Tishkevich, A.V. Trukhanov, S.V. Trukhanov, J. Cryst. Growth 626 (2024) 127481.
[16] A.V. Trukhanov, V.A. Turchenko, V.G. Kostishin, F. Damay, F. Porcher, N. Lupu, B. Bozzo, I. Fina, S. Polosan, M.V. Silibin, M.M. Salem, D.I. Tishkevich, S. V. Trukhanov, J. Alloy. Compd. 886 (2021) 161249.
[17] R.E. El-Shater, H. El Shimy, S.A. Saafan, M.A. Darwish, D.i. Zhou, K.C.B. Naidu, M. U. Khandaker, Z. Mahmoud, A.V. Trukhanov, S.V. Trukhanov, F. Fakhry, Mater. Adv. 4 (2023) 2794–2810, https://doi.org/10.1039/d3ma00105a.
[18] S.V. Trukhanov, A.V. Trukhanov, S.G. Stepin, H. Szymczak, C.E. Botez, Magn. Ferroelectricity 50 (2008) 886–893.
[19] S. Nair, M. Deshpande, V. Shah, S. Ghaisas, S. Jadkar, J. Phys. Condens. Matter. 31 (44) (2019) 445902.
[20] R. Yao, T. Zhou, S. Ji, W. Liu, X. Li, Molecules 28 (18) (2023) 6601.
[21] R. Zhihui, X. Zhao, X. Gong, Adv. Funct. Mater. (2024) 2406424.
[22] P. Blaha, K. Schwarz, G.K.H. Madsen, D. Kvasnicha, J. Luitz, WIEN2k, An Augmented Plane Wave + Local Orbitals Program for Calculating Crystal Properties, Karlheinz Schwarz, Techn. Universitate Wien, Austria, 2001.
[23] J.P. Perdew, K. Burke, M. Ernzerhof, Phys. Rev. Lett. 77 (1996) 3865.
[24] A.D. Becke, E.R. Johnson, A Simple Effective Potential for Exchange, American Institute of Physics, 2006.
[25] A.E. Mattsson, P.A. Schultz, M.P. Desjarlais, Designing meaningful density functional theory calculations in materials science-Aprimer, Model. Simul. Mater. Sci. Eng. 13R (2005) 1.
[26] R. Hoppe, B. Hofmann, Z. Für Anorg. Allg. Chem. 436 (1977) 65–74.
[27] R. Ullah, M.A. Ali, K.M. Katubi, N.S. Alsaiari, K.M. Abualnaja, A.S. Verma, G. Murtaza, Inorg. Chem. Commun. 139 (2022) 109315.
[28] S.A. Mir, D.C. Gupta, RSC Adv. 10 (2020) 26277.
[29] M. Faizan, S.H. Khan, A. Khan, A. Laref, G. Murtaza, Int. J. Modern Phys. B 32 (2018) 1850270.
[30] M. Faizan, S.H. Khan, G. Murtaza, A. Khan, A. Laref, Int. J. Modern Phys. B 33 (09) (2019) 1950072.
[31] S.S. Grabchikov, A.V. Trukhanov, S.V. Trukhanov, I.S. Kazakevich, A.A. Solobay, V.T. Erofeenko, N.A. Vasilenkov, O.S. Volkova, A. Shakin, J. Magn. Magn. Mater. 398 (2016) 49–53.
[32] S.V. Trukhanov, A.V. Trukhanov, A.N. Vasiliev, A.M. Balagurov, H. Szymczak, J. Exp. Theor. Phys. 113 (2011) 819–825.
[33] V. Sherrington, S. Kirkpatrick, Phys. Rev. Lett. 35 (1975) 1792.
[34] H. Szymczak, M. Baran, J. Fink Finowicki, J. Magn. Magn. Matter. (2004, 1327,) 272–276.
[35] Y. Kumar, K.L. Yadav, J. Shah, R.K. Kotnala, J. Adv. Ceram. 8 (3) (2019) 333–344. ISSN 2226-4108 DOI: 10.1007/s40145-019-0315-7 CN 10-1154/T.
[36] S.V. Trukhanov, A.V. Trukhanov, A.N. Vasiliev, A.M. Balagurov, H. Szymczak, J. Exp. Theor. Phys. 113 (5) (2011) 819–825.
[37] S.V. Trukhanov, A.V. Trukhanov, A.N. Vasiliev, H. Szymczak, J. Exp. Theor. Phys. 111 (2010) 2.